Investigating atmospheric predictability on Mars using breeding vectors in a general-circulation model

Journal Item

Q. J. R. Meteorol. Soc. (2004), **130**, pp. 2971–2989 doi: 10.1256/qj.03.209

Investigating atmospheric predictability on Mars using breeding vectors in a general-circulation model

By C. E. NEWMAN*, P. L. READ and S. R. LEWIS
University of Oxford, UK

(Received 17 November 2003; revised 13 April 2004)

SUMMARY

A breeding vectors approach is used to investigate the hypothesis that the Martian atmosphere is predictable at certain times of year, by identifying the fastest-growing modes of instability at different times in a Mars general-circulation model. Results indicate that the period from northern mid-spring until mid-autumn is remarkably predictable, with negative global growth rates for a range of conditions, in contrast to the situation on the earth.

From northern late autumn to early spring growing modes do occur, peaking in northern high latitudes and near winter solstice. Reducing the size of the initial perturbations increases global growth rates in most cases, supporting the idea that instabilities which saturate nonlinearly at lower amplitudes have generally faster growth rates. In late autumn/early winter the fastest-growing modes ('bred vectors') are around the north pole, increase with dust loading, and probably grow via barotropic as well as baroclinic energy conversion. In northern late winter/early spring the bred vectors are around the north pole and are strongly baroclinic in nature. As dust loading (and with it the global circulation strength) is increased their growth rates first decrease, as the baroclinic mode is suppressed, then increase again as the fastest-growing instabilities switch to being those which dominated earlier in the year. If dust levels are very low during late northern autumn (late southern spring) then baroclinic modes are also found around the spring pole in the south, though for a slight increase in dust loading the dominant modes shift back to northern high latitudes.

The bred vectors are also used as perturbations to the initial conditions for ensemble simulations. One possible application within the Mars model is as a means of identifying regions and times when dust-lifting activity (related to surface wind stress) might show significant interannual variability for a given model configuration, without the need to perform long, computationally expensive multi-year model runs with each new set-up. This is tested for a time of year when previous multi-year experiments showed significant variability in dust storm onset in the region north of Chryse. Despite the model having no feedbacks between dust lifting and atmospheric state (unlike the original multi-year run), the ensemble members still show maximum divergence in this region in terms of near-surface wind stress, suggesting both that this application deserves further testing, and that the intrinsic atmospheric variability alone may be important in producing interannual variability in this storm type.

KEYWORDS: Ensemble methods Planetary science

1. INTRODUCTION

Despite many large differences, such as a hundredfold lower atmospheric density, a CO_2 atmosphere able to condense onto the polar caps and 'thermal continents' rather than oceans, there are also a great many similarities between Mars and the earth. Heat is transported by the atmosphere, though at a lesser rate on Mars owing to Mars's lower densities. Owing to its thin nature and resulting fast radiative time-scales, the distribution of temperature on Mars is far more strongly linked to variations in solar insolation, with the sub-solar latitude generally the warmest region on the planet rather than the equator. Thus, although Hadley circulations are present as on the earth, with two cells rising near the equator near equinox, a single cross-equatorial cell exists near solstice as a consequence of the greatest heating being located well into the summer hemisphere. Zonal-mean surface wind patterns are linked to these large circulations, with baroclinic instability and strong midlatitude weather systems also present, as on earth (see e.g. Zurek 1992; Barnes *et al.* 1993).

During northern late autumn and winter, large (planet-encircling or even global) dust storms occur on Mars in some years, resulting in very stable lapse rates in the lower atmosphere and an expansion of the meridional circulation as atmospheric

* Corresponding author, present affiliation: California Institute of Technology, Mail Code 150-21, 1200 E. California Blvd., Pasadena, CA 91125, USA. e-mail: claire@gps.caltech.edu

heating increases. The size, onset location and timing of such storms is highly variable from year to year, and produces the greatest interannual variability in the Martian climate (Zurek and Martin 1993). Observations (e.g. Barnes 1980, 1981) and general-circulation model results (e.g. Collins *et al.* 1996) suggest, however, that the Martian atmosphere is sometimes capable of showing a high degree of regularity, and potentially of repeatability and predictability. If the latter were to be true, then it would represent a major difference between the Martian and terrestrial atmospheres, as such predictability is not observed for the earth (see discussion in section 3(a)).

This paper attempts for the first time to quantify the predictability of the Martian atmosphere, using a technique known as 'breeding vectors' which provides a way of identifying the fastest-growing modes of instability in the atmosphere and their growth rates (Toth and Kalnay 1993). These modes or 'bred vectors' take the form of the final perturbation field after several breeding cycles (discussed in section 2(b)), and negative growth rates indicate an atmosphere which is highly stable with respect to perturbations. Section 2 describes the Mars general-circulation model used in this work and gives an outline of the breeding vectors technique, then describes the detailed application of this within the model. Several factors affect the bred vectors and growth rates produced, including the initial perturbation amplitudes and the atmospheric dust loading used in the model. Section 3 describes the bred vectors obtained in experiments conducted using a moderately dusty model atmosphere, with first large then smaller initial perturbation amplitudes used to assess the impact of this choice. Section 4 then examines the effect of using different dust loadings, using first a clear (no dust) then a very dusty atmosphere.

For times of year when growing modes do exist, it is desirable to perform an ensemble of experiments (rather than a single, deterministic forecast) when trying to predict the atmospheric state at some point in the future. The bred vectors are the modes which have grown most rapidly in the recent past, thus providing an optimal estimate of the range of possible initial states for the ensemble experiments (e.g. Toth and Kalnay 1997). Once several sets of bred vectors have been produced, each set can be used as the initial perturbation for a different ensemble member. This differs slightly from using singular vectors of the tangent linear system (e.g. Molteni *et al.* 1996), which are those modes expected to grow most rapidly in the near future, and hence are explicitly aimed at maximizing the range of possible outcomes (though here the use of a tangent linear model rather than the full nonlinear model must also be taken into consideration). Section 5 describes a test of one possible application of the ensemble technique within the Oxford Mars general-circulation model, as a way of looking for likely regions and times of interannual variability without needing to actually perform long, multi-year simulations.

2. Methodology

(*a*) *The Oxford-LMD Mars general-circulation model (MGCM)*

The Oxford-LMD Mars general-circulation model (MGCM) consists of a dynamical core (horizontally spectral and vertically finite difference in the Oxford version) and a comprehensive set of parametrizations of subgrid-scale physical processes. (LMD stands for the Laboratoire de Météorologie Dynamique du Centre National de la Recherche Scientifique, France.) The physical processes parametrized include radiative transfer, gravity-wave and low-level form drag, a ten-layer soil scheme, vertical diffusion and convective adjustment, CO_2 condensation and sublimation, and dust lifting, atmospheric transport and deposition (Forget *et al.* 1999; Newman *et al.* 2002a). In all results shown later, the Oxford version was used with a horizontal resolution of

$5° \times 5°$, and with 25 vertical levels extending from ~5 m above the surface to ~90 km (as described by Lewis *et al.* 1999). The 'terrain-following' σ coordinate is used in the vertical, where $\sigma =$ pressure/surface pressure, and is particularly necessary for Mars with its huge (tens of kilometres) variations in topographic height—height or pressure levels would be problematic, as they would intersect much of the surface. The Martian year is split for convenience into 12 seasons or months, equally spaced in areocentric longitude L_s. This is the angle between the sun's position and its position at northern spring equinox, hence $L_s = 0°$, 90°, 180° and 270° correspond to northern spring equinox, summer solstice, autumn equinox and winter solstice, and to the start of months 1, 4, 7 and 10, respectively.

Atmospheric dust has a substantial impact on the state of the Martian atmosphere (e.g. Gierasch and Goody 1972). In its absence, little solar radiation is directly absorbed by the atmosphere, whereas dust absorbs solar as well as scattering and emitting thermal radiation, leading to a warmer atmosphere and generally colder surface if more dust is aloft. It is therefore important for the dust distribution to be realistic in order to simulate a realistic model state. Ideally, the dust distribution would evolve according to parametrizations of dust lifting, advection, mixing and gravitational sedimentation, all of which are dependent in turn on the model state. It is possible to run the MGCM with all these interdependencies present, allowing feedbacks between, for example, dust lifting and low-level wind stress, with higher wind stresses enabling more dust to be lifted into the atmosphere, changing the local temperature and wind structure and (if enough is raised) affecting the strength of the global circulation (Newman *et al.* 2002b). Breeding vectors will be applied to such versions of the MGCM in the future. Currently, however, such versions can generally only provide semi-realistic dust distributions and hence model states. Moreover, the threshold-sensitive nature of the dust-lifting parametrizations, combined with potentially strong feedbacks, means that results are likely to be very sensitive to exact choices of start time, dust-lifting parameters, etc., and hence open up a far wider regime range than is desirable in a first application of this technique to Mars. The results that follow therefore use the MGCM with a number of prescribed dust distributions which, although generally less spatially and temporally variable than actual distributions found on Mars, are designed to produce realistic model states.

(*b*) *The breeding vectors technique*

Breeding vectors is a technique used to identify the fastest-growing modes of instability in a nonlinear model. Such modes or 'bred vectors' are the perturbations to the atmospheric state which exist at the end of a breeding run, and are related to Lyapunov vectors, which are commonly used to study the growing modes of a system. If an infinitesimally small random perturbation is added to a dynamical field, the leading Lyapunov vector after some time is the direction of growth with the greatest growth rate (given by the Lyapunov exponent). Bred vectors are defined similarly, except that the initial perturbation is of a finite size and the bred vectors are produced by renormalizing the size of the perturbations (if the total becomes larger than its initial value) at regular intervals (Kalnay *et al.* 2002). The reason for both differences is that bred vectors are designed to work in nonlinear models, where nonlinear saturation will occur when the perturbations reach some finite amplitude. The idea is thus to choose an initial total perturbation amplitude which is sufficiently large that modes which grow rapidly but saturate at relatively low amplitudes (so are likely to be unimportant in a weather-prediction sense) will saturate during each 'breeding cycle', while more significant modes, which saturate at larger amplitudes, continue to grow. At the end of each

breeding cycle downwards renormalization occurs if necessary, which prevents the latter set of modes from ever reaching saturation.

Obvious parameters over which there is some freedom of choice are the length of the breeding cycle and the size of the initial total perturbation, and these are of clear importance since they will determine which modes are included and which are effectively removed by saturation. This is an advantage of the breeding vectors technique, and has been explored and used to good effect in various earth applications (Toth and Kalnay 1993, 1997; Cai *et al.* 2003). Another choice to be made is the method by which the total perturbation amplitude is calculated—options include, for example, the weighted global-mean stream function squared or potential enstrophy (potential vorticity squared). While studies using earth GCMs (e.g. Corazza *et al.* 2003) indicate that the choice has little impact, this has still to be determined for other planets with different dynamical regimes.

(*c*) *Implementing breeding vectors in the MGCM*

The total size of the global perturbation, ψ, is calculated from stream-function perturbations in the MGCM, i.e. the renormalization required is determined with regard to this variable and hence a 'stream-function norm' is used (though different norms will be tested in the future). The steps are as follows:

(i) Perform a control run C, outputting fields of surface pressure P_s, zonal wind u, meridional wind v and temperature T as well as the stream function Ψ, with an output frequency equal to the length of one breeding cycle in the perturbation run.

(ii) Begin a perturbation run P with almost identical initial conditions to those of C, but with the T field perturbed using white-noise perturbations of a selected mean size, and with the u and v fields adjusted to provide a nearly balanced initial state.

(iii) Find the initial value of ψ (the square root of the globally summed area- and mass-weighted stream-function perturbation squared):

$$\psi = \sqrt{\sum_i \{A(i)(M_P(i)\Psi_P(i) - M_C(i)\Psi_C(i))\}^2},$$

where $A(i)$ is the area weighting required and $M(i)$ the mass weighting required for grid point i, $\Psi_C(i)$ and $\Psi_P(i)$ are the stream function at grid point i in the control and perturbation runs, respectively, and where the sum is over all model grid points.

(iv) After one breeding cycle has elapsed (e.g. 6 hours) find the new value of ψ and hence the renormalization parameter $\nu = \psi(t = 0)/\psi(t)$.

(v) If ν is less than 1 the total size of the perturbations has increased and they must be renormalized (see later).

(vi) After renormalization, continue 'breeding' (repeating steps (iv) and (v)) until the end of the breeding run (which may be, for example, 10 to 30 days).

The renormalization involves calculating new values of the atmospheric variables for run P ($P_{s,P}$, u_P, v_P and T_P) such that, for example,

$$u_P(i, t)_{new} - u_C(i, t) = \nu(u_P(i, t)_{old} - u_C(i, t)).$$

(*d*) *Calculating growth rates*

Following a breeding run consisting of several breeding cycles, daily global growth rates may be calculated by assuming that growth within a breeding cycle is given by

$$\psi(t + \delta t) = \psi(t)\, \mathrm{e}^{\kappa \delta t},$$

where κ = growth rate. Hence the daily growth rate is given by

$$\kappa = \log\{\psi(t + \delta t)_{\mathrm{new}}/\psi(t)\}/\delta t,$$

where $\delta t = 1$ sol, $\psi(t)$ is the global-mean perturbation at the start of the sol, and $\psi(t + \delta t)_{\mathrm{new}}$ is an approximation of the global-mean perturbation which would have been produced by the end of the sol if no renormalizations had been performed*. If the renormalization factor ν was less than 1, for any of the breeding cycles during each sol of the breeding run, then a renormalization was performed to reset ψ to $\psi(t = 0)$ on each occasion (the same as multiplying by ν). Hence $\psi(t + \delta t)_{\mathrm{new}}$ is found by dividing $\psi(t + \delta t)$ by all ν values within the sol which were less than 1.

3. Results using the 'Viking' dust scenario

The 'Viking' dust scenario was designed to produce a model atmosphere similar to that inferred from lander data obtained during the Viking Mars missions (e.g. Zurek and Martin 1993), though with the two global storm peaks of 1977 smoothed out to a great extent. The scenario is described in detail in Lewis *et al.* (1999), but its key features are a gradual increase in visible dust opacity (normalized to the 700 Pa level, which is necessary as surface pressure varies from 300 to 1300 Pa), from 0.4 at $L_{\mathrm{s}} = 100°$ (in northern summer) to 1.0 at $L_{\mathrm{s}} = 280°$ (in southern summer). This scenario probably produces a slightly dustier and hence warmer atmosphere than is typically found on Mars at the present time. The peak coincides roughly with the time at which the southern hemisphere receives the greatest heating relative to the north. Aided by dynamical effects, this results in the strongest circulations being produced, and hence stronger near-surface winds which lift larger amounts of dust into the atmosphere (Haberle *et al.* 1982; Newman *et al.* 2002b). Dust loading falls off roughly exponentially with height, with the top of the dust layer lower over the poles than the equator, and highest during the dustiest periods (varying between 20 km at the poles during clear months and 78 km at the equator during dusty months). The breeding vectors method was applied to each month in turn, using initial white-noise temperature perturbations with a mean size of first 5 K then 1 K, with breeding cycles lasting 6 Mars hours and with a total breeding time of 30 sols.

(*a*) *Large-amplitude perturbations*

Figure 1 shows daily global growth rates over the entire 30 sol period for each month, with the average over sols 4 to 30 summarized in Table 1, for experiments using mean initial perturbation amplitudes of 5 K. The results demonstrate clearly the lack of growing modes for over half of the year, from northern spring equinox until after autumn equinox. Figure 1 also shows that, while there is continuous growth of perturbations in months 9 and 10, there are periods of decay in months 8, 11 and 12 despite these showing net growth overall.

The results suggest that the Martian atmosphere should be quite predictable in months 1 to 7 (northern mid-spring to mid-autumn), in contrast to the behaviour seen

* A sol is a Martian solar day.

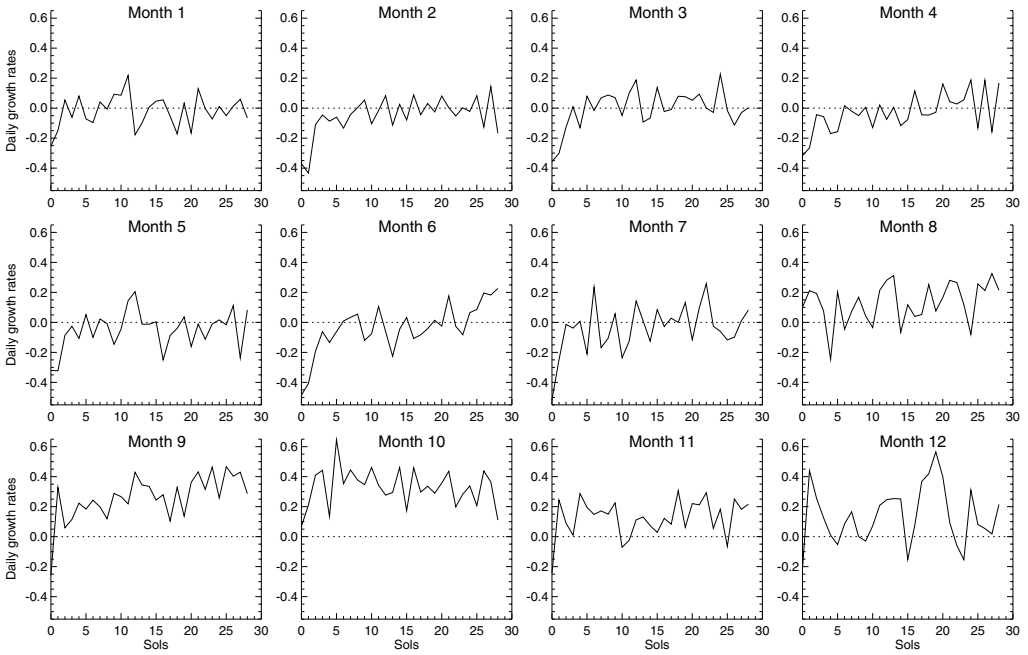

Figure 1. Daily global growth rates for all 12 months using the Viking dust scenario and relatively large mean initial temperature perturbation amplitudes of 5 K.

TABLE 1. GROWTH RATES USING THE VIKING DUST SCENARIO

Month	Time of year	Mean daily growth rate
1	Northern mid-spring	−0.0197
2		−0.0495
3		−0.00308
4	Northern mid-summer	−0.0307
5		−0.0494
6		−0.0363
7	Northern mid-autumn	−0.0376
8		0.130
9		0.262
10	Northern mid-winter	0.330
11		0.126
12		0.140

Mean daily global growth rates, averaged over sols 4 to 30 of a breeding run in each month, using the Viking dust scenario and relatively large mean initial temperature perturbation amplitudes of 5 K.

in the earth's atmosphere. In terrestrial models for which the breeding technique is used operationally for ensemble forecasting, no days have been found to have negative growth rates over a hemispheric or global domain (Zoltan Toth 2003, personal communication). Experiments conducted by the authors, using a version of the United Kingdom Met Office's Unified Model (Cullen 1993), have also found only positive growth rates on a global scale for all times of year examined.

Figure 2 shows the normalized bred vectors at four model levels in months 9 and 10, i.e. during northern hemisphere winter when growth rates are at their maximum. These therefore represent the fastest-growing modes of instability which do not saturate at the typical amplitudes allowed by the choice of 5 K initial mean perturbation amplitudes. 'Normalized' here means that the pressure-weighted perturbation (difference in stream function between runs C and P) at each height level is shown divided by the area- and pressure-weighted global-mean value (i.e. ψ). Figure 3 shows the same but for months 11 and 12, i.e. late northern winter/early northern spring. In all months shown, the scale of the bred modes is large compared to results obtained for the earth. This reflects the fact that, while low zonal wave-number waves typically dominate in the Martian atmosphere (produced, for example, by baroclinic instabilities or via interactions between the strong wave-number-3 topography and the thermal tide), on the earth smaller structures are more common owing to strong smaller-scale forcing (e.g. from land–sea contrasts) and processes related to atmospheric water vapour (such as 'storm tracks'). Added to this, while the Rossby radius of deformation is similar on Mars and earth, the smaller radius of Mars means that fewer waves can fit around a latitude circle. Smaller-scale structures may become more important if the Mars model is run at greater resolution, though this has not yet been explored.

Figures 2 and 3 both show bred vectors confined to northern mid- to high latitudes, more so later in the year, with little structure in the south. The main difference between the results shown in Fig. 3 and those in Fig. 2 is the concentration of the bred modes at lower levels. The contour intervals are tripled for Fig. 3 (amplitudes for 30 or 50 km are not shown as they are too low to show up with the same contour intervals), whereas in the middle of winter (Fig. 2) the modes extended up through most levels, peaking at $\sim$30 km in month 10.

In the later months, e.g. month 12, the bred vectors can be clearly identified as baroclinic modes with zonal wave number $m = 2$, which are found to be travelling eastwards with a period of $\sim$4.3 sols. Their baroclinic nature is demonstrated in Fig. 4 which shows longitude–height cross-sections of the bred perturbations for months 10 and 12. The right column (month 12) shows clearly that these perturbations tilt westwards with height, which is the behaviour expected of waves which grow via the baroclinic conversion of energy. This is expected to be the dominant form of instability in situations where pressure and density surfaces are tilted with respect to each other (associated with vertical wind shear by thermal wind balance), as is the case during early northern spring when large horizontal temperature gradients exist around the extensive north polar cap.

The modes may be related to atmospheric waves which are present in the simulations. Figure 5 shows the dominant wave amplitudes present in the model atmosphere during month 12, obtained using a Fourier analysis of the model temperature field over 30 sols. As well as an $m = 2$, period 4.3 sols wave, two strong $m = 1$ waves are also present, with periods 4.3 and 6 sols. These waves are more vertically extended than the $m = 2$ wave, which is confined below $\sim$30 km as are the corresponding bred vectors. This analysis indicates therefore that, although $m = 1$ wave amplitudes dominate at this time of year, they are probably highly predictable, and that the greatest response to atmospheric perturbations and hence variability occurs in terms of changes in $m = 2$ wave amplitude.

It should be noted that the dominant waves produced by the model are in good agreement with observed wave amplitudes and periods for this time, found in surface pressure data obtained by the Viking Landers (Barnes 1980; Barnes *et al.* 1981), for which the $m = 2$ wave shows up relatively strongly as it peaks near the surface, and in

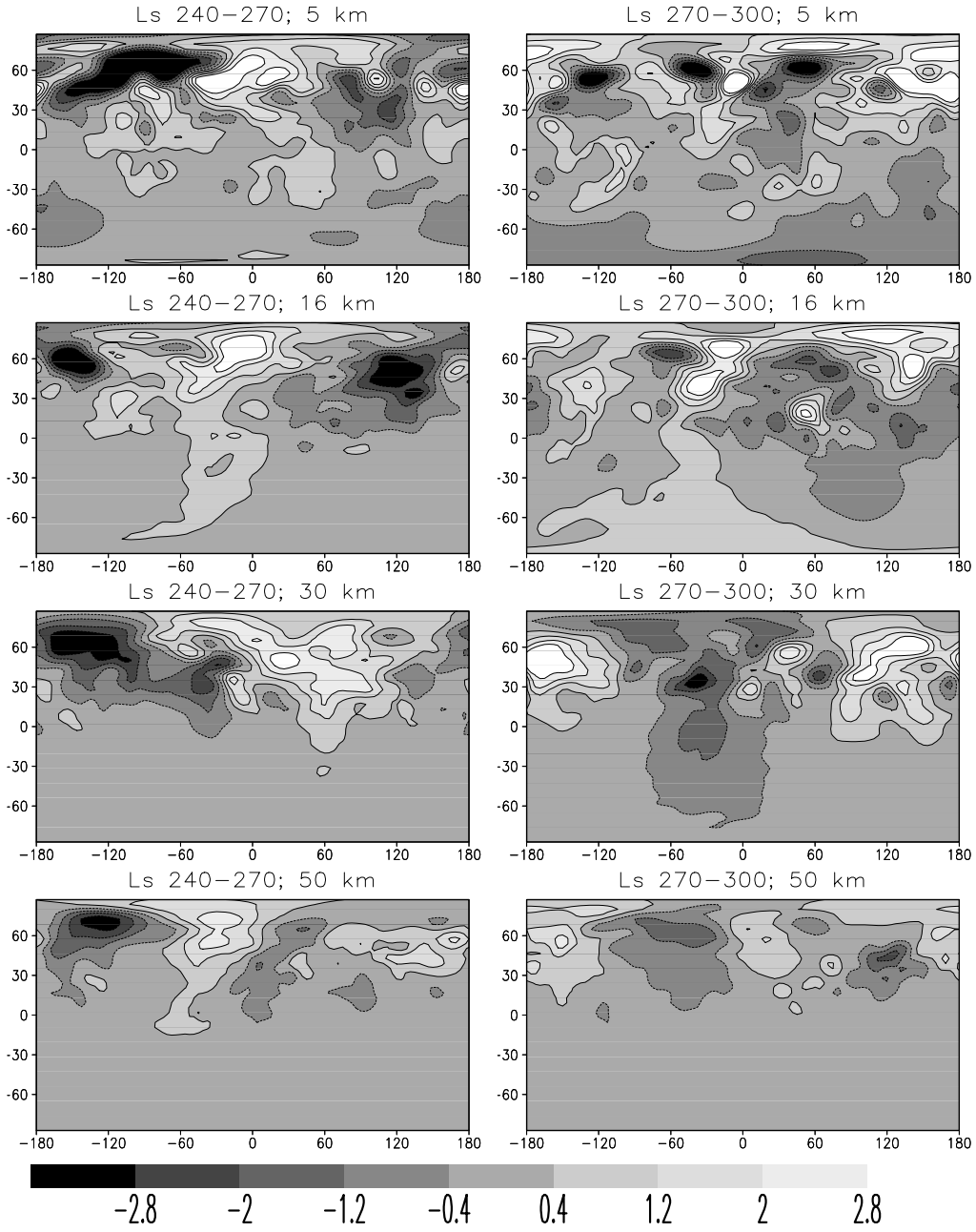

Figure 2. Normalized stream-function perturbations at the end of a 30-sol breeding run for northern winter months 9 (left) and 10 (right) on four model levels (average heights shown) using the Viking dust scenario and relatively large mean initial temperature perturbation amplitudes of 5 K.

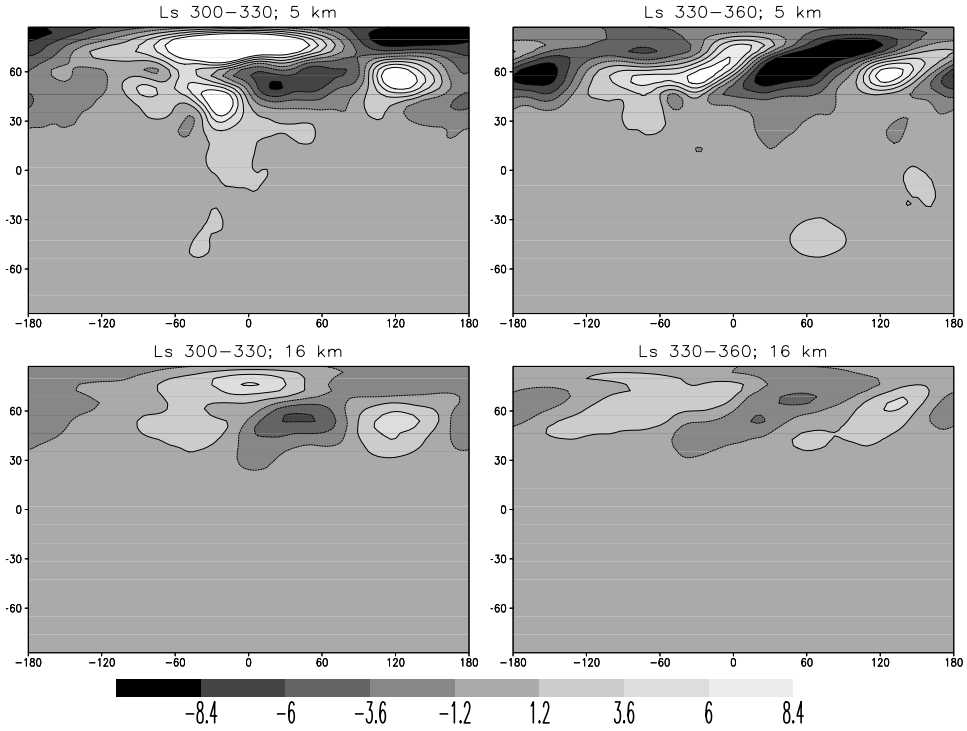

Figure 3. As in Fig. 2 but for northern late winter months 11 and 12, and showing results for 5 and 16 km only.

temperature data from the Thermal Emission Spectrometer on the Mars Global Surveyor orbiter (MGS TES) (Wilson *et al.* 2002), in which the two $m = 1$ waves are found to be more vertically extended and to be the dominant modes at higher altitudes.

The bred vectors produced in month 10 are more complex and harder to identify. The left column of Fig. 4 shows longitude–height cross-sections of the bred perturbations at this time, and these no longer show a westward tilt with height, suggesting that they grow via barotropic or more complicated barotropic/baroclinic energy conversion. As shown in Fig. 2, the dominant zonal wave number of fastest growth (of the bred vectors) is no longer clearly 2, but rather a mixture of $m = 1$, 2 and 3.

The largest-amplitude waves present in the simulation for month 10 are shown in Fig. 6. The largest of these have $m = 1$, are vertically and meridionally extended (reaching to equatorial latitudes aloft) and have longer periods than the $m = 1$ modes found for month 12. Peak amplitudes occur high over polar regions, and are greater than during the later month. Waves with very similar characteristics have recently been identified in northern winter MGS TES data. Wilson *et al.* suggest that these are Rossby waves, centred in a midlatitude wave guide established by the circumpolar jet and largely drawing energy from the mean flow via barotropic energy conversion (though with some evidence of baroclinic conversion within the jet core). The observed mode disappears rapidly after month 10, which is again in agreement with the bred vectors produced. Thus the fastest-growing modes of instability in month 10, a time of year when the meridional circulation and circumpolar jet are at their strongest, may be a mixture of planetary waves competing to grow via these mechanisms.

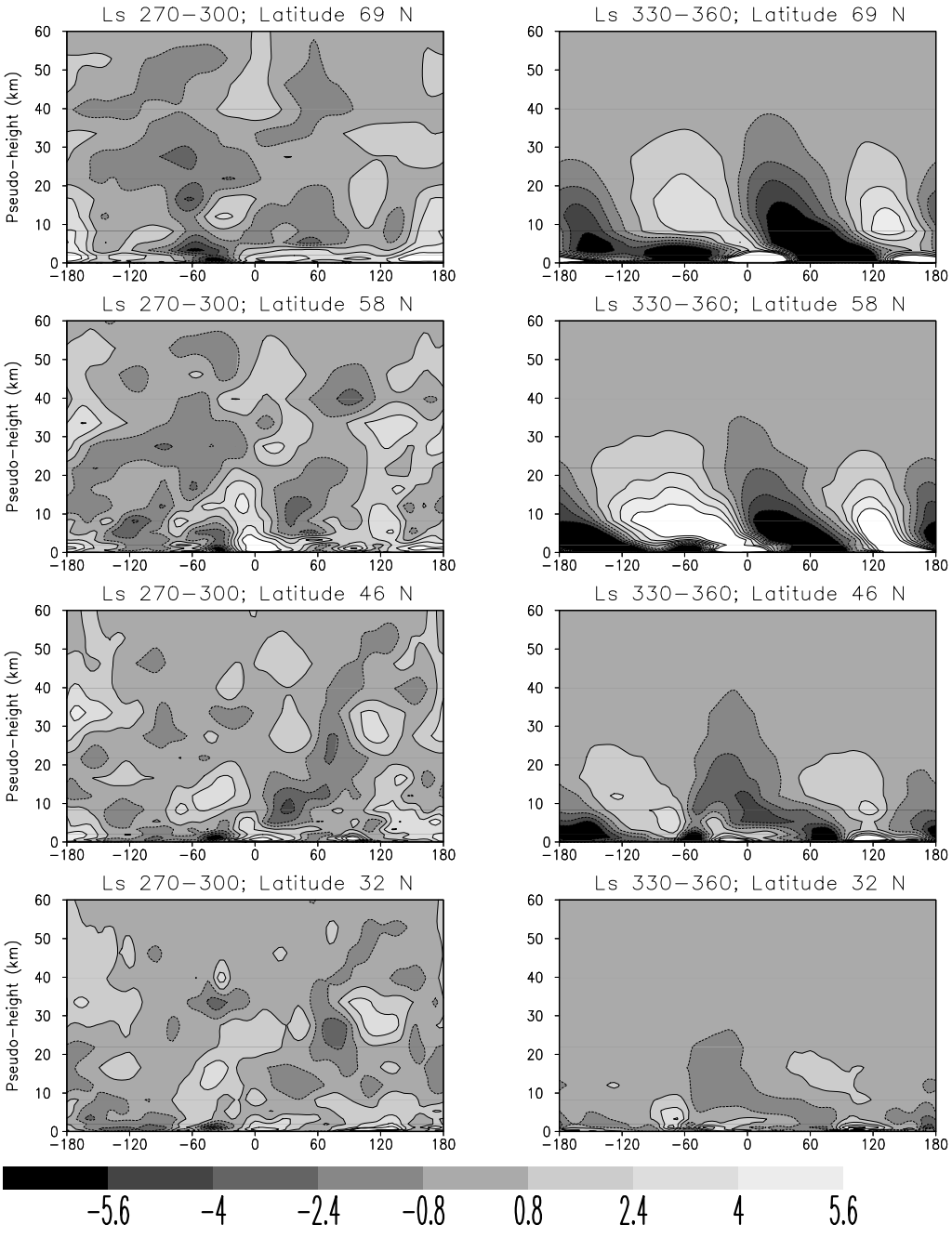

Figure 4. Longitude–height plots of normalized stream-function perturbations at the end of a 30-sol breeding run for months 10 (northern winter, left) and 12 (northern early spring, right) at four northern latitudes using the Viking dust scenario and relatively large mean initial temperature perturbation amplitudes of 5 K. The vertical axis is labelled with the σ coordinate described in section 2(a).

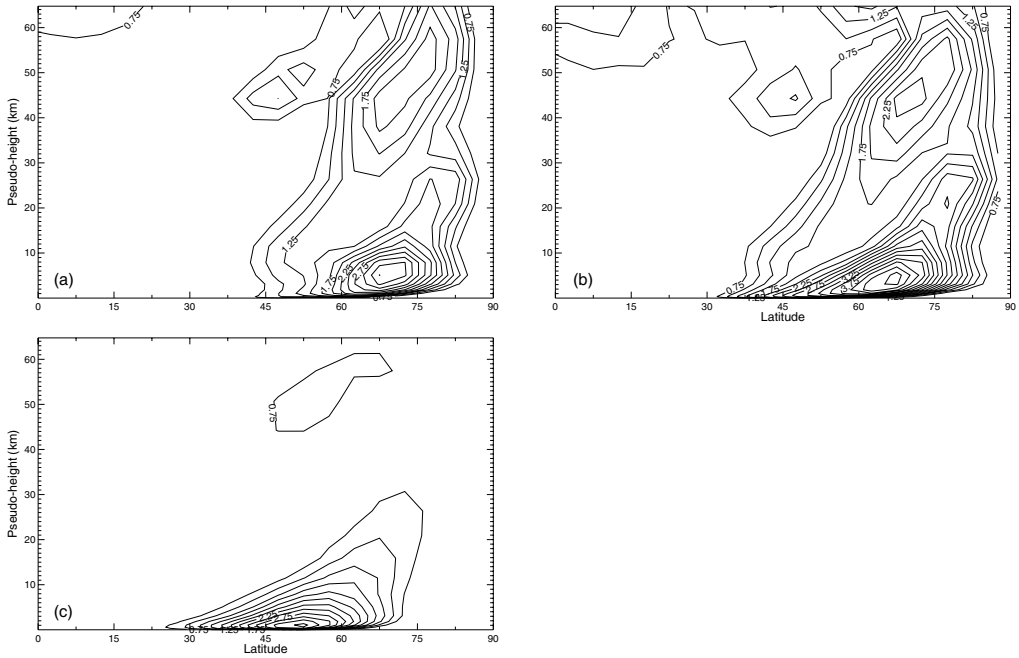

Figure 5. Northern hemisphere temperature wave amplitudes (K) for eastward travelling waves in the month 12 Viking dust simulation for: (a) zonal wave number 1, period 4.29 sols; (b) zonal wave number 1, 6.00 sols; (c) zonal wave number 2, 4.29 sols.

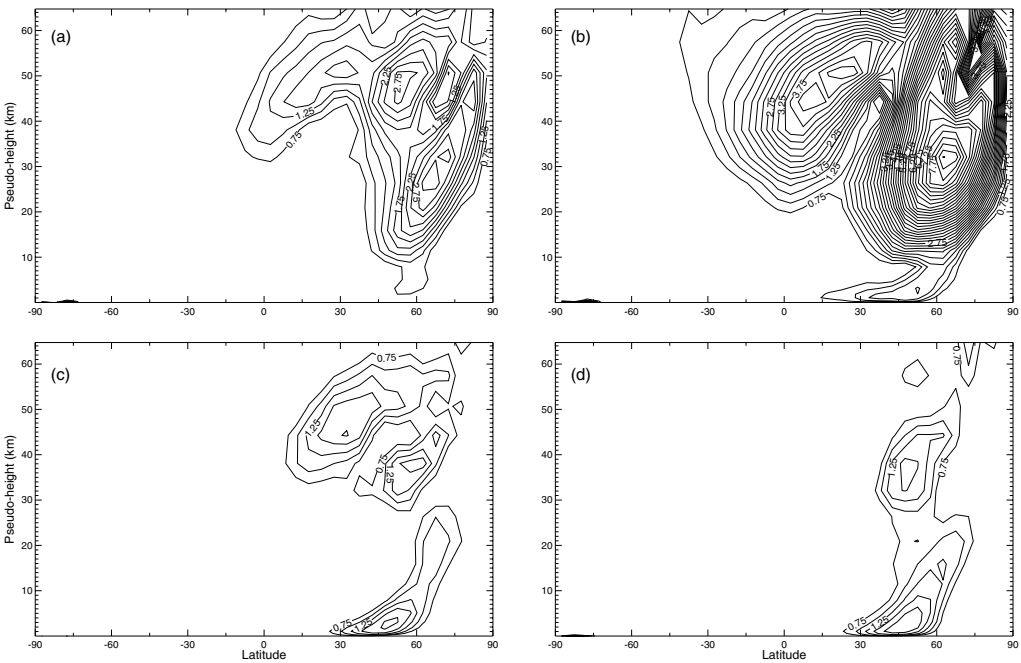

Figure 6. Temperature wave amplitudes (K) for eastward travelling waves in the month 10 Viking dust simulation for: (a)–(b) zonal wave number 1; (c)–(d) zonal wave number 2. The period for (a) and (c) is 6 sols, and for (b) and (d) is 10 sols.

TABLE 2. GROWTH RATES USING DIFFERENT PERTURBATION AMPLITUDES

Month	Mean daily growth rate for large perturbation amplitudes	Mean daily growth rate for small perturbation amplitudes
1	−0.0197	−0.00355
8	0.130	0.704
10	0.330	1.99
12	0.140	0.112

As in Table 1 but showing results for the two mean initial perturbation amplitudes and for fewer months.

When independent breeding cycles are performed, the phases and amplitudes of the leading local Lyapunov vectors (of which the bred modes are superpositions) are random, which ensures quasi-orthogonality among the global bred vectors (Toth and Kalnay 1997). Results are not shown here for independent breeding cycles, though this was explored by performing the experiments a number of times using different initial perturbations. There are distinct differences in the details of the month 9 bred modes produced using different initial perturbations, though their general description remains the same. In month 12, however, the modes produced by different breeding runs differ in more straightforward ways, with (apart from slight amplitude changes) most differences being easily attributable to a phase change in one or more of the main wave numbers involved.

(*b*) *Smaller-amplitude perturbations*

Using smaller perturbations (here with a mean value of 1 K) results in renormalization being performed before modes which saturate at smaller amplitudes have reached saturation, hence these can continue to grow. Given that such modes would be expected to grow more rapidly and be greater in number, growth rates are expected to increase relative to those shown earlier. Changing the length of the breeding cycles is also expected to have an impact, in that renormalization occurs earlier or later, thus respectively allowing a smaller or greater number of modes to reach saturation prior to renormalization—in these experiments, however, a breeding cycle period of 6 hours was found in general to produce the greatest growth rates, for both the larger and smaller perturbation amplitudes, as compared with results for cycles lasting either 2 or 12 hours.

Table 2 shows growth rates for the original and smaller initial perturbation amplitudes for a selection of months around northern winter. Mean growth rates are still negative for months 1 to 7 (northern spring to early autumn) although, as shown for month 1, the rate of decay is generally reduced. In most cases where there is overall growth, the use of smaller initial perturbations produces an increase in growth rate. In month 10, near solstice, the amplitudes would increase by seven times (according to the simple formula) every sol in the absence of renormalization (though of course without renormalization they would saturate fairly rapidly). The exception is month 12, for which growth is reduced when the perturbations are smaller. This suggests that more complicated nonlinear effects than simple saturation are involved for sufficiently large amplitudes.

The structure of the modes produced is also different to that found using larger initial perturbations, with generally smaller spatial scales and with more structure at lower latitudes. Earth-based experiments show a similar trend as initial perturbation amplitudes are decreased (Toth and Kalnay 1997), due to the increasing importance of convective instabilities, which peak in the Tropics.

TABLE 3. GROWTH RATES USING DIFFERENT DUST SCENARIOS

Month	Mean daily growth rate for clear conditions	Mean daily growth rate using Viking dust	Mean daily growth rate for very dusty conditions
8	0.316	0.130	0.482
10	0.148	0.330	1.261
12	0.230	0.140	0.149

As in Table 1 but showing results for three months around northern winter and for three dust scenarios.

4. RESULTS USING OTHER DUST SCENARIOS

As described earlier, the dust loading has a significant impact on the atmospheric circulation and stability. The greatest variability in dust loading, in terms of global or large-scale dustiness, occurs between late southern spring and early southern autumn, i.e. months 8 to 12, and depends on the number and size of major storms which occur during that time. To explore the changes in bred modes due to this variability, further experiments were performed in months 8, 10 and 12. The first set uses a totally dust free, clear atmosphere, representing an extreme situation which is unlikely to occur in reality even in the absence of any major storms. The second set uses the same vertical dust distribution, and latitudinal variation of dust-top height, as in the Viking scenario, but with a constant visible dust opacity at 700 Pa of 4.0. In months 8, 10 and 12 alike, the global opacity normalized to the 700 Pa surface is therefore four times larger than the maximum reached in the Viking scenario (during month 10), representing the dust loading encountered during global storms (though month 12 is after the peak in storm activity, hence such opacities are unlikely). This is also an extreme case.

Results are shown in Table 3. Near solstice (month 10), growth rates increase with atmospheric dust content. The theory of simple baroclinic instability in the Martian atmosphere (e.g. Barnes 1984; Zurek *et al.* 1992) predicts instead that wave amplitudes should decrease as dust levels and hence static stability increase. The mechanism suggested by Wilson *et al.* (2002) to explain observed waves in northern winter may be consistent with amplitudes increasing during times of increased dust loading, although they note that further work is underway to examine the sensitivity of these modes to changes in dust loading and the associated strength of the Hadley circulation. Later in the year (month 12), growth rates are greater for a clearer atmosphere, and the bred modes show a similar tilt with height to those in the right column of Fig. 4, with larger amplitudes at higher levels than for the Viking dust scenario. This does fit with ideas of baroclinic waves becoming stronger for clear conditions, when static stabilities are lower. Growth rates do also increase slightly for the very dusty situation in month 12, but in this case they have lost their strong baroclinic character, and resemble the modes found in month 10. Incidentally, in section 3(a) the results for month 6 were produced using a clearer atmosphere than those for month 12 (month 12 opacities being almost 50% larger in the observations-based Viking dust scenario), yet even with this bias mean growth rates for month 6 were negative. Hence, early northern spring does appear to be more baroclinically unstable than the opposite time of year, even though dust levels are generally higher at this time, in agreement with results from the MGCM and other models (e.g. Barnes *et al.* 1993).

Earlier in the year (month 8), growth rates are greatly increased for higher dust levels, as was the case for month 10, but they also increase when the dust is removed entirely. This coincides with the location of fastest-growing instability switching from

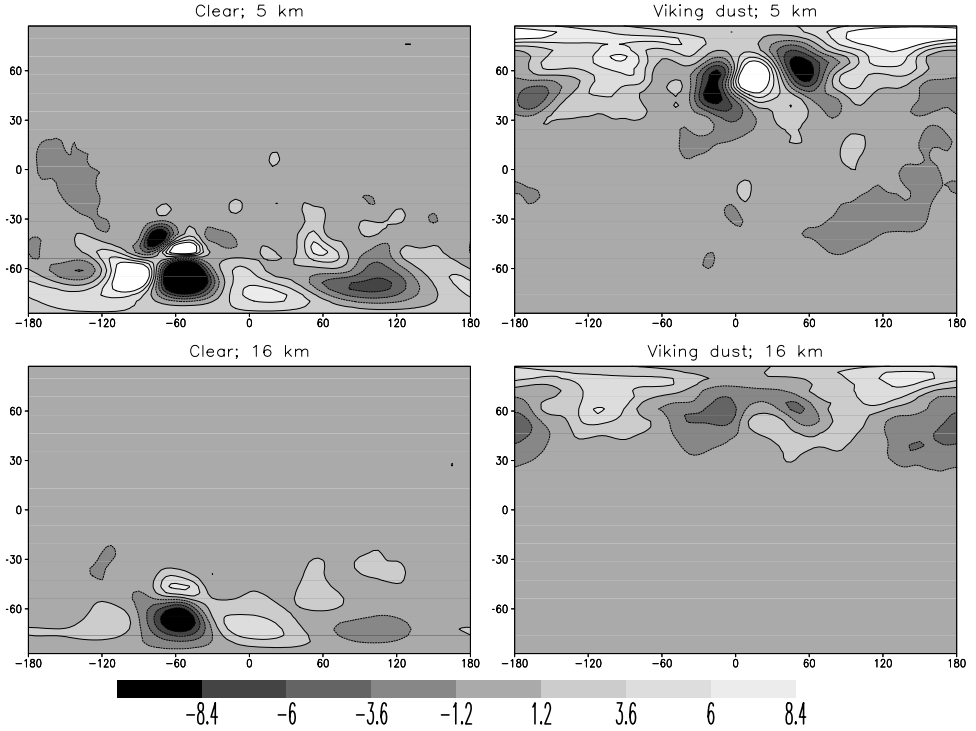

Figure 7. As in Fig. 2 but for month 8 (late southern spring) for a clear atmosphere (left) and with Viking dust (right), and showing results for 5 and 16 km only.

southern to northern high latitudes as the atmosphere becomes dustier. Figure 7 demonstrates this by showing month 8 normalized perturbations for the clear and Viking cases. Looking at the vertical structure of the southern high-latitude bred modes for the clear case, they are clearly baroclinic in structure, similar to those found in the north for Viking dust conditions (and also for the clear case, not shown) in month 12. Hence, southern late spring and northern early spring are both susceptible to fast-growing baroclinic instabilities in the spring hemisphere provided the atmospheric dust load is small enough.

5. Investigating variability in dust storm initiation using ensemble techniques: a test case

In Newman *et al.* (2002b), the main source of interannual variability in the most realistic model run (using wind-stress lifting as the primary mechanism and with active dust transport) was a regional dust storm in the Chryse region (∼0–60°W, ∼10°S–25°N). The model was run for 11 full Mars years in total, yet the storm occurred only in years 1 and 10, at $L_s \sim 255°$ and 240°, respectively. The storm developed from local dust-lifting activity (due to the wind-stress mechanism) just north of the Chryse region, and its onset and evolution closely resembled one observed at a similar time of year ($L_s \sim 224°$) on Mars itself (Cantor *et al.* 2001; Smith *et al.* 2001; Newman *et al.* 2002b). One goal of future work with the MGCM is to represent more of the interannual variability observed on Mars, which may be lacking in the model because of, for example, insufficient resolution or incorrect/incomplete parametrizations of dust

lifting or other physical processes. A major problem in determining the effect of any model changes is the time required to perform numerous multi-annual simulations, which must then be analysed to look for increased variability in terms of storm type, size and duration. It would therefore be useful if ensemble simulations could be performed at key times of year (i.e. during months 8–11, when Mars shows the greatest variability in regional/global storm production) to assess the likely spread of possible outcomes, without actually needing to run the MGCM continuously for multiple years. The following describes a preliminary test of this method's ability to predict regions of dust storm variability in the MGCM, using breeding vectors to produce the initial perturbations required for each ensemble member (as discussed in section 1).

The ensemble simulation was performed at the same time of year as the simulated Chryse storms, and near-surface wind stresses compared after 10 sols to determine whether dust lifting by the wind-stress mechanism would vary significantly between the ensemble members. The aim was to see if the ensemble experiment could predict the interannual variability present in the 11-year active dust run. The test is made more challenging by the fact that the MGCM version used here (with prescribed dust) is missing an important component which probably contributes strongly to interannual variability on Mars—feedbacks between dust lifting, the dust distribution and the atmospheric state. Thus if this ensemble simulation using the MGCM with prescribed dust indicates significant differences in dust lifting between ensemble members, and their locations correlate with year-to-year differences in the 11-year active dust run at this time of year, it suggests that at least some of the interannual variability present in the latter is due to intrinsic atmospheric variability alone.

The experiment used 12 ensemble members, each initialized with bred modes produced using different initial random perturbations. The bred modes were taken from the end of a 10-sol breeding run begun at $L_s = 240°$, with 6-hour breeding cycles. In the 11-year active dust run of Newman *et al.* (2002b) the simulated dust distribution produced by this time of year was closer to the clear case than the Viking scenario. With this in mind, the simply prescribed dust loading for these ensemble experiments consisted of constant visible opacities everywhere of 0.2 at 700 Pa and the dust top everywhere set to ∼30 km. Figure 8 shows the difference between each ensemble member and the ensemble mean in terms of the near-surface wind stress, 10 sols into the ensemble run. The difference field has clear peaks in the region ∼ 0°–60°W, 20°–50°N, indicating that in this region (just north of Chryse) wind stresses show the greatest variability (outside high northern latitudes). Differences in wind stress between ensemble members are up to 20% of the maximum wind stresses found in this region (∼0.024 N m^{-2}). Threshold wind stresses for dust lifting to occur were calculated separately for each grid point in the active dust run of Newman *et al.* (2002b), but averaged over this area were also ∼0.024 N m^{-2}. Such variations would therefore be capable of producing a significant difference in the amount of dust injected (a difference which would then be amplified by positive feedbacks in a simulation with radiatively active dust transport, e.g. Newman *et al.* 2002b).

These results indicate the potential for using ensemble techniques in searching for times and regions of likely interannual variability in dust-lifting activity, though further tests are required, not only with the prescribed dust MGCM but also with the active dust model version (once breeding vectors have been tested here). The results also indicate that variability in the atmospheric circulation alone (i.e. without dust feedbacks present) probably contributed to the modelled (Newman *et al.* 2002b) variability in the initiation of dust lifting north of the Chryse area in early northern winter. The initial onset of dust lifting may be due to fortuitous combinations of different flow regimes so as to enhance

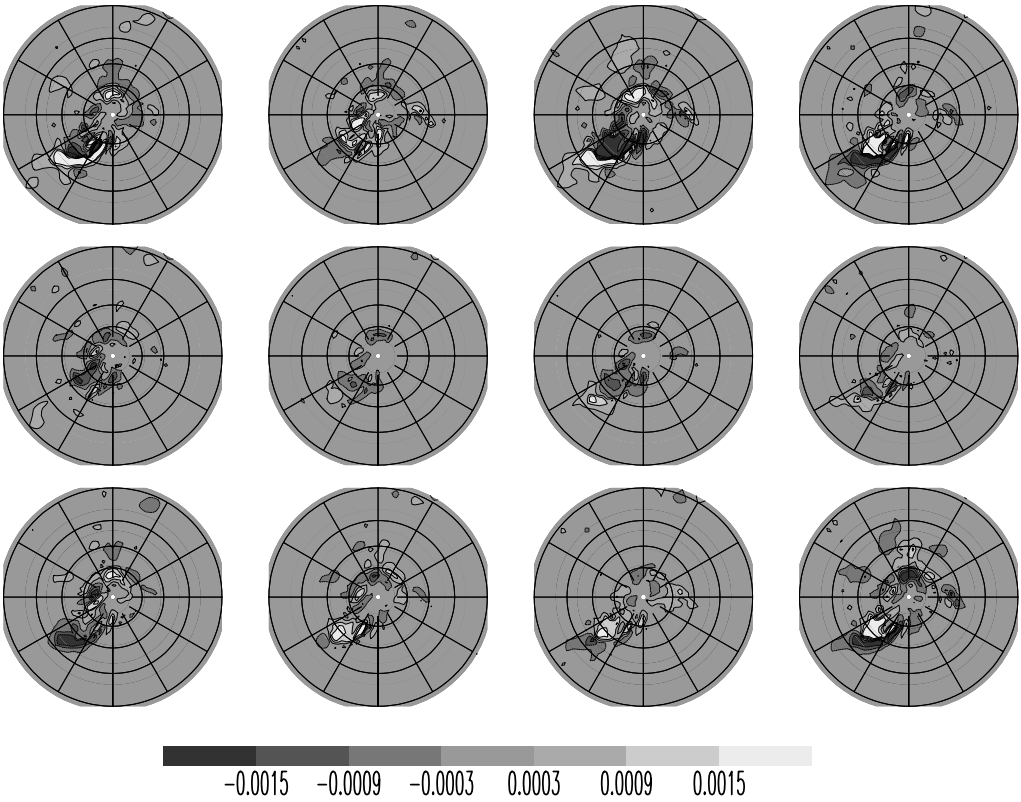

Figure 8. Each plot is for a different ensemble member, showing the difference between its near-surface wind stress (N m^{-2}) and the ensemble mean value, 10 sols into the ensemble run. The polar stereographic projections are for the northern hemisphere (0°–90°N) with the 0°, 20°, 40° and 60° latitude circles shown. (No features would be visible in the southern hemisphere for the selected contour intervals.) The 0° longitude is at the bottom of each circle, with 30° longitude intervals indicated by the straight lines.

near-surface wind magnitudes (e.g. baroclinic waves and slope winds). Interannual variability could then also arise from a lack of repeatability in these regimes, such as the phases of the baroclinic waves differing from year to year (see e.g. Wang *et al.* 2003). Incidentally, if the Viking dust scenario is used for the ensemble runs then Chryse no longer appears as a region of maximum divergence between ensemble members. The reason for this is the reduction in baroclinic activity caused by the increased dust opacity, which results in wind stresses in the Chryse region being lower, and more controlled by other factors.

The MGCM (with or without active dust transport) has not yet produced significant interannual variability in terms of other storm types, hence other tests of this method, as applied to dust storm initiation, are not yet possible. Work is ongoing to solve this problem, and to thus produce a model which is more Mars-like. Tests have, however, been performed to check that the method does not produce false positives in regions which, though having high modelled wind stresses, also have low modelled interannual variability. For example, peak wind stresses in months 9, 10 and 11 in the southern hemisphere (particularly around the Hellas basin) are comparable with those north of Chryse in early month 9, but in a series of ensemble experiments these locations show almost no difference in near-surface wind stress between ensemble members. This is in

good agreement with the results of long simulations which show strong repeatability in terms of dust lifting around Hellas from year to year, and demonstrates that peak wind stresses do not simply equate to large wind-stress differences.

6. Summary and conclusions

Observations and models suggest that the Martian atmosphere may be predictable at certain times of year. A breeding-vectors approach has been used to investigate this hypothesis, by identifying the fastest-growing modes of instability at different times in a Mars general-circulation model. Results indicate that the period from northern mid-spring until mid-autumn is remarkably predictable in this model. Perturbations to the model state decay with time, and there are no growing modes found for a range of sizes of initial perturbations/lengths of breeding cycles. This result is therefore quite different to that which is obtained in the earth's atmosphere. One possible caveat is that the atmospheric dust distribution used in the model, though realistic, is prescribed, precluding feedbacks between the atmospheric state and the dust cycle, which may increase variability when included. During this period such effects are likely to be small, however, as it is observed to be a time of minimal dust storm activity, with highly repeatable dust loadings from year to year. A further point is that the sensitivity of results to model resolution has not yet been explored. The results of early experiments conducted at a lower horizontal resolution ($\sim 7.5°$ in latitude and longitude) are in agreement with these conclusions, but it is at higher resolutions that more differences might be expected, due for example to the improved representation of small-scale topography and the associated atmospheric response.

From northern late autumn, through winter and until early spring, growing modes are found to be present, mostly in northern high latitudes and peaking near winter solstice. In general, instabilities which saturate nonlinearly at lower amplitudes have faster growth rates. Reducing the size of the initial perturbations reduces the amplitude a given instability can attain before it is renormalized, hence the faster-growing modes described can continue to grow without saturating, and mean global growth rates should increase. This is the case for most of the conditions shown above, with the exception of early northern spring (month 12) for which growth rates are reduced for smaller initial perturbations.

In northern late autumn and winter the fastest-growing modes (with high growth rates which increase with dust loading) are around the north pole, and are probably Rossby waves growing via barotropic as well as baroclinic energy conversion. Provided dust loadings are below certain levels, northern late winter/early spring (months 11 and 12) and at least late southern spring (month 8) show the fastest-growing modes to be around the winter/spring pole and strongly baroclinic in nature. These have lower growth rates, which increase as dust loading is reduced, in agreement with simple baroclinic instability theory. Above a certain dust level, however, the modes and growth rates produced behave more as for northern winter, with only a moderate atmospheric dust loading required to shift from fastest growth in southern baroclinic modes to northern 'mixed modes' for month 8. Thus these 'mixed modes' appear to dominate, producing fast-growing instabilities in northern midlatitudes to high latitudes, provided the dust loading is large enough to force a strong global-scale circulation, though the exact details of this process are not yet known.

Bred vectors have been used as initial conditions for ensemble MGCM simulations, to test a possible application in searching for regions and times of potential interannual variability for a given model configuration. Peak variability in near-surface wind stress

(in terms of the position of maximum divergence between ensemble members) is found just north of the Chryse region during early northern winter, coinciding with a time and place on Mars where regional storm onset is variable between years in both observations and models. The fact that significant divergence was found between ensemble members, despite no dust feedbacks being present, suggests that interannual variability in the atmosphere alone may affect the initial production of storm clouds here, rather than requiring positive feedbacks between wind stresses and dust lifting (though the latter effect is almost certainly key to producing further storm development).

The MGCM used here was run with a prescribed dust distribution, which prevented feedbacks between dust lifting, the dust distribution and atmospheric state. The next step will be to examine the impact, on predictability and on the fastest-growing modes produced, of using radiatively active dust transport within the atmosphere. This enables feedbacks between the atmospheric state and dust distribution, allowing, for example, longitudinal asymmetries to appear in the dust load, affecting wave forcing within the atmosphere. A major step will then be to include parametrized dust lifting, enabling the full range of feedbacks. As dust lifting by near-surface wind stress is thought to be a threshold process on Mars, small changes to the atmospheric state can lead to huge differences, and it is therefore likely that an analysis of the fastest-growing modes and growth rates will prove more difficult in such circumstances, and that in ensemble experiments the members may diverge considerably. In spite of this, however, it is possible that the Martian atmosphere may still be classed as highly predictable during much of the northern spring to autumn period, as dust lifting tends to be minimal during this time.

Acknowledgements

The authors would like to thank Zoltan Toth and Eugenia Kalnay for helpful discussions, comments and enthusiasm, two anonymous reviewers for thought-provoking suggestions, and gratefully acknowledge support for this work from the UK Particle Physics and Astronomy Research Council.

References

Barnes, J. R. 1980 Time spectral analysis of midlatitude disturbances in the Martian atmosphere. *J. Atmos. Sci.*, **37,** 2002–2015

1981 Midlatitude disturbances in the Martian atmosphere: A second Mars year. *J. Atmos. Sci.*, **38,** 225–234

1984 Linear baroclinic instability in the Martian atmosphere. *J. Atmos. Sci.*, **41,** 1536–1550

Barnes, J. R., Pollack, J. B., Haberle, R. M., Leovy, C. B., Zurek, R. M., Lee, H. and Schaeffer, J. 1993 Mars atmospheric dynamics as simulated by the NASA Ames General Circulation Model. II—Transient baroclinic eddies. *J. Geophys. Res.*, **98,** 3125–3148

Cai, M., Kalnay, E. and Toth, Z. 2003 Bred vectors of the Zebiak–Cane model and their potential application to ENSO predictions. *J. Climate*, **16,** 40–56

Cantor, B. A., James, P. B., Caplinger, M. and Wolff, M. J. 2001 Martian dust storms: 1999 Mars Orbiter Camera observations. *J. Geophys. Res.*, **106 E10,** 23653–23687

Collins, M., Lewis, S. R., Read, P. L. and Hourdin, F. 1996 Baroclinic wave transitions in the Martian atmosphere. *Icarus*, **120,** 344–357

Corazza, M., Kalnay, E., Patil, D. J., Szunyogh, I., Hunt, B. R., Ott, E. and Yorke, J. A. 2003 Use of the breeding technique to estimate the structure of the analysis 'errors of the day'. *Nonlinear Processes in Geophys.*, **10,** 233–243

Cullen, M. J. P. 1993 The unified forecast/climate model. *Meteorol. Mag.*, **122,** 81–94

Forget, F., Hourdin, F., Fournier, F., Hourdin, C., Talagrand, O., Collins, M., Lewis, S. R., Read, P. L. and Huot, J.-P. 1999 Improved general circulation models of the Martian atmosphere from the surface to above 80 km. *J. Geophys. Res.*, **104,** 24155–24175

Gierasch, P. J. and Goody, R. M. 1972 The effect of dust on the temperature structure of the Martian atmosphere. *J. Atmos. Sci.*, **29,** 400–402

Haberle, R. M., Leovy, C. and Pollack, J. B. 1982 Some effects of global dust storms on the atmospheric circulation of Mars. *Icarus*, **50,** 322–367

Kalnay, E., Corazza, M. and Cai, M. 2002 'Are bred vectors the same as Lyapunov vectors?' Pp. 173–177 in Proceedings of AMS Symposium on observations, data assimilation and probabilistic prediction, 12–17 January 2002. American Meteorological Society, 45 Beacon Street, Boston MA02108-3693, USA

Lewis, S. R., Collins, M., Read, P. L., Forget, F., Hourdin, F., Fournier, F., Hourdin, C., Talagrand, O. and Huot, J.-P. 1999 A climate database for Mars. *J. Geophys. Res.*, **104,** 24177–24194

Molteni, F., Buizza, R., Palmer, T. N. and Petroliagis, T. 1996 The ECMWF ensemble prediction system: Methodology and validation. *Q. J. R. Meteorol. Soc.*, **122,** 73–119

Newman, C. E., Lewis, S. R., Read, P. L. and Forget, F. 2002a Modeling the dust cycle in a Mars general circulation model. 1: Representations of dust transport processes. *J. Geophys. Res.*, **107 E12,** doi: 10.1029/2002JE001910

2002b Modeling the dust cycle in a Mars general circulation model. 2: Multi-annual radiatively active dust transport simulations. *J. Geophys. Res.*, **107 E12,** doi: 10.1029/2002JE001920

Smith, M. D., Pearl, J. C., Conrath, B. J. and Christensen, P. R. 2001 Thermal Emission Spectrometer results: Atmospheric thermal structure and aerosol distribution. *J. Geophys. Res.*, **106 E10,** 23929–23946

Toth, Z. and Kalnay, E. 1993 Ensemble forecasting at NMC—the generation of perturbations. *Bull. Am. Astron. Soc.*, **74,** 2317–2330

1997 Ensemble forecasting at NCEP and the breeding method. *Monthly Weather Rev.*, **125,** 3297–3319

Wang, H., Richardson, M. I., Wilson, R. J., Ingersoll, A. P., Toigo, A. D. and Zurek, R. W. 2003 Cyclones, tides, and the origin of a cross-equatorial dust storm on Mars. *Geophys. Res. Lett.*, **30**(9), doi: 10.1029/2002GL016828

Wilson, R. J., Banfield, D., Conrath, B. J. and Smith, M. D. 2002 Traveling waves in the northern hemisphere of Mars. *Geophys. Res. Lett.*, **29**(14), doi: 10.1029/2002GL014866

Zurek, R. W. 1992 'Comparative aspects of the climate of Mars: An introduction to the current atmosphere'. Pp. 799–817 in *Mars*. Eds. H. H. Kieffer, B. M. Jakosky, C. W. Snyder and M. S. Matthews, The University of Arizona Press, Tuscon and London

Zurek, R. W. and Martin, L. J. 1993 Interannual variability of planet-encircling dust activity on Mars. *J. Geophys. Res.*, **98,** 3247–3259

Zurek, R. W., Barnes, J. R., Haberle, R. M., Pollack, J. B., Tillman, J. E. and Leovy, C. B. 1992 'Dynamics of the atmosphere of Mars'. Pp. 835–933 in *Mars*. Eds. H. H. Kieffer, B. M. Jakosky, C. W. Snyder and M. S. Matthews, The University of Arizona Press, Tuscon and London